

Herschel discovery of far-infrared emission from the hot spot D in the radio galaxy Cygnus A

Yuji Sunada,¹★ Naoki Isobe,² Makoto S. Tashiro,^{1,2} Motoki Kino,^{3,4} Shoko Koyama,^{5,6} and Satomi Nakahara²

¹ Department of Physics, Saitama University, 255 Shimo-Okubo, Sakura-ku, Saitama, 338-8570, Japan

² Institute of Space and Astronautical Science (ISAS), Japan Aerospace Exploration Agency (JAXA),

3-1-1 Yoshinodai, Chuo-ku, Sagami-hara, Kanagawa, 252-5210, Japan

³ Kogakuin University of Technology & Engineering, Academic Support Center, 2665-1 Nakano, Hachioji, Tokyo 192-0015, Japan

⁴ National Astronomical Observatory of Japan, 2-21-1 Osawa, Mitaka, Tokyo, 181-8588, Japan

⁵ Niigata University, 8050 Ikarashi-nino-cho, Nishi-ku, Niigata 950-2181, Japan

⁶ Institute of Astronomy and Astrophysics, Academia Sinica,

11F of Astronomy-Mathematics Building, AS/NTU No. 1, Sec. 4, Roosevelt Rd, Taipei 10617, Taiwan, R.O.C.

Accepted XXX. Received YYY; in original form ZZZ

ABSTRACT

The far infrared counterpart of hot spot D, the terminal hot spot of the eastern jet hosted by the radio galaxy Cygnus A, is detected with *Herschel* Aperture photometry of the source performed in 5 photometric bands covering the wavelength range of 70–350 μm . After removing the contamination from another nearby hot spot, E, the far-infrared intensity of hot spot D is derived as 83 ± 13 and 269 ± 66 mJy at 160 and 350 μm , respectively. Since the far-infrared spectrum of the object smoothly connects to the radio one, the far-infrared emission is attributed to the synchrotron radiation from the radio-emitting electron population. The radio-to-near-infrared spectrum is confirmed to exhibit a far-infrared break feature at the frequency of $\nu_{\text{br}} = 2.0^{+1.2}_{-0.8} \times 10^{12}$ Hz. The change in energy index at the break ($\Delta\alpha = 0.5$) is interpreted as the impact of radiative cooling on an electron distribution sustained by continuous injection from diffusive shock acceleration. By ascribing the derived break to this cooling break, the magnetic field, B , in the hot spot is determined as a function of its radius, R within a uniform one-zone model combined with the strong relativistic shock condition. An independent B - R constraint is obtained by assuming the X-ray spectrum is wholly due to synchrotron-self-Compton emission. By combining these conditions, the two parameters are tightly determined as $B = 120$ – 150 μG and $R = 1.3$ – 1.6 kpc. A further investigation into the two conditions indicates the observed X-ray flux is highly dominated by the synchrotron-self-Compton emission.

Key words: magnetic fields – acceleration of particles – radiation mechanism; non-thermal – galaxies: jets – infrared: galaxies – galaxies: individual: Cygnus A

1 INTRODUCTION

Hot spots of Fanaroff-Riley type-II (FR-II; Fanaroff & Riley 1974) radio galaxies are compact and bright radio structures located where their jets terminate (Meisenheimer et al. 1989). It is widely thought that particles are efficiently accelerated into the relativistic regime in the hot spots via the diffusive shock acceleration (or the so-called Fermi-I process e.g., Bell 1978), as observationally evidenced by their synchrotron radiation (Meisenheimer et al. 1989). Thus, the hot spots are frequently proposed as one of the possible production sites of ultra-high-energy cosmic rays (Hillas 1984; Kotera & Olinto 2011). For detailed investigation into the particle acceleration phenomena in the hot spots, it is important to measure their magnetic field strength since it is theoretically predicted to be one of the ma-

jor parameters which control the particle acceleration and associated cooling efficiencies.

Since pioneering discoveries of X-ray emission from a number of hot spots with *ROSAT* and *Chandra* (Harris et al. 1994; Wilson et al. 2000; Harris et al. 2000; Hardcastle et al. 2001, 2002), a comparison between the radio and X-ray fluxes has been the standard method to evaluate their magnetic field for more than two decades. The radio and X-ray spectra of these hot spots are widely interpreted by the one-zone Synchrotron-Self-Compton (SSC; Band & Grindlay 1985) process (e.g., Hardcastle et al. 2004; Kataoka & Stawarz 2005), except for a few optical hot spots (e.g., Wilson et al. 2001; Hardcastle et al. 2004). These studies indicate a typical magnetic field of $B = 100$ – 500 μG in the hot spots, which implies nearly equipartition value as $B/B_{\text{eq}} \sim 0.1$ – 2 . In addition, the SSC analysis, in combination with detailed investigation of the shock dynamics, was theoretically applied to infer the energetics and plasma composition in the hot spots, and hence, in the jets of the FR-II radio galaxies (e.g.,

★ E-mail: sunada@heal.phy.saitama-u.ac.jp

Kino & Takahara 2004; Godfrey & Shabala 2013; Snios et al. 2018; Croston et al. 2018; Sikora et al. 2020).

It is not necessarily well recognised that the standard method is often accompanied by a "hidden" uncertainty. The synchrotron and SSC intensities are mainly dependent on the following three physical quantities; i.e., the magnetic field, electron energy density and size of the emission region (Band & Grindlay 1985). From measurements of the radio and X-ray fluxes alone, it is not possible to disentangle these three parameters. Thus, the observed radio and X-ray spectra are inevitably reproduced by the SSC model with different parameter sets (Wilson et al. 2000; Kino & Takahara 2004; Stawarz et al. 2007). In order to overcome this difficulty, the apparent source size is usually estimated by making use of high-resolution images. However, for some hot spots, a difference by more than a factor of two is found among measurements on the source size due to the different observational configurations (e.g., Perley et al. 1984; Wilson et al. 2000). This results in a notable uncertainty in the magnetic field estimation. Therefore, we need to search for another observational indicator of the magnetic field and/or the source size of the hot spots.

We propose to adopt a synchrotron spectral feature, called the "cooling break", to be observed in the frequency range higher than the radio one as the third item of observational information to constrain the magnetic field and size of the hot spots. In the case of the diffusive shock acceleration under a continuous energy injection condition, the spectrum of the accelerated electrons is predicted to exhibit a break at the Lorentz factor for which the radiative cooling time scale is balanced with the adiabatic loss one (Meisenheimer et al. 1989; Carilli et al. 1991). As a result, the synchrotron spectrum is expected to break similarly at the corresponding frequency. This cooling break is utilised to estimate the magnetic field and source size (Inoue & Takahara 1996; Kino & Takahara 2004). In fact, the cooling break is successfully adopted to model the multi-frequency spectra of blazars (e.g. Kataoka et al. 2000). Because the hot spots and blazars are widely considered to share injection and cooling processes, the hot spots are expected to exhibit inevitably the cooling break in their synchrotron spectrum.

From synchrotron studies of several archetypical hot spots in the near-infrared (NIR) to the optical bands (Meisenheimer et al. 1997; Kraft et al. 2007; Werner et al. 2012), their cooling break is suggested to be located in the far-infrared (FIR) band, namely $10^{11} - 10^{12}$ Hz (Brunetti et al. 2003; Cheung et al. 2005). However, their radio-to-optical spectrum is alternatively interpreted by the spectral cut-off feature corresponding to the maximum electron energy, rather than the break one, so far. A definite observational evidence of the cooling break in the spectrum of the hot spots has remained unexplored, because a wide spectral gap around the FIR band in the spectrum of the hot spots prevents from discriminating between the two spectral features.

In order to search for the cooling break of the hot spots, the Spectral and Photometric Imaging REceiver (SPIRE; Griffin et al. 2010) and Photodetector Array Camera and Spectrometer (PACS; Poglitsch et al. 2010) onboard the *Herschel* space observatory (Pilbratt et al. 2010) provides an ideal tool. A combination of these two instruments operated in the photometer mode covers a wide FIR wavelength range of $70 - 500 \mu\text{m}$, corresponding to the frequency range of $(0.6 - 4.3) \times 10^{12}$ Hz, where the hot spots are typically expected to exhibit the cooling break as mentioned above. Thanks to their reasonable photometrical sensitivity (typically $\gtrsim 10$ mJy) and moderate angular resolution (about 20 and 10 arcsec for SPIRE and PACS, respectively), these two instruments are applicable to the hot spots with a projected distance from its nucleus of larger than a few arcmin. In fact, the FIR emission from the western hot spot of the

representative FR-II radio galaxy Pictor A was discovered with the *Herschel* SPIRE (Isobe et al. 2020).

The hot spot named "D" of the FR-II radio galaxy Cygnus A (Carilli & Barthel 1996), located at the end of its eastern jet (Bentley et al. 1975; Perley et al. 1984) is one of the best candidates for the FIR studies with *Herschel*. This hot spot has been extensively observed in radio, NIR and X-ray bands (Meisenheimer et al. 1989; Carilli et al. 1991; Wilson et al. 2000; Wright & Birkinshaw 2004; Stawarz et al. 2007). Its radio-to-X-ray spectrum is usually explained by the SSC process (Harris et al. 1994; Wilson et al. 2000; Stawarz et al. 2007). By artificially introducing a possible cooling break at the frequency of 0.5×10^{12} Hz into the SSC model, Stawarz et al. (2007) estimated the magnetic field strength of the hot spot as $B = 270 \mu\text{G}$ for the radius of $R = 0.8$ kpc. The observed properties of hot spot D are utilised to investigate the properties of the jets, lobes and cocoons of this radio galaxy (e.g., Wilson et al. 2006; Yaji et al. 2010). Analytical and theoretical studies tried to evaluate the dynamics, energetics and plasma composition related to the jets, by connecting the physical quantities observed from the above components (e.g., Smith et al. 2002; Kino & Kawakatu 2005; Ito et al. 2008; Kino et al. 2012; Steenbrugge et al. 2014; Kawakatu et al. 2016; Snios et al. 2018). However, as mentioned above, due to the FIR spectral gap in $10^{11} - 10^{13}$ Hz, the cooling break has not yet been observationally confirmed, and there probably remain notable uncertainties in the physical parameters of the hot spot. From its relatively high radio flux density of ~ 10 Jy at 10 GHz and radio energy index of $\alpha \sim 1$, the FIR flux density of the hot spot is estimated as ~ 100 mJy at 10^{12} Hz, which is significantly higher than the SPIRE and PACS sensitivities. Because of its large angular separation from the nucleus of Cygnus A, of ~ 50 arcsec, hot spot D is safely detectable by the two instruments without suffering from any nuclear contamination. Therefore, we investigate the FIR infrared spectrum of the hot spot to make sure of its cooling break, by utilising the *Herschel* SPIRE and PACS data.

For direct comparison, we adopt the same cosmological constants as those in Stawarz et al. (2007) throughout the present paper; i.e., $H_0 = 71 \text{ km s}^{-1} \text{ Mpc}^{-1}$, $\Omega_m = 0.27$, $\Omega_\Lambda = 0.73$. At the redshift of Cygnus A ($z = 0.05607$; Owen et al. 1997), the luminosity distance is evaluated as 248 Mpc. The angular size of 1 arcsec corresponds to the physical size of 1.07 kpc at the source rest frame.

2 OBSERVATION AND ANALYSIS

2.1 *Herschel* Data

In order to investigate the FIR properties of the hot spot of Cygnus A, we utilised the FIR data obtained with the PACS and SPIRE photometers. The SPIRE photometer mapped Cygnus A on 2011 October 11 in the Large Map mode (Obs. ID of 1342230853), while the PACS photometers observed the object on 2011 December 24 with two pairs of cross-scan mappings, at a scan speed of 20 arcsec s^{-1} . In the first cross-scan observation (Obs. ID of 1342235110 and 1342235111), the blue camera of the PACS photometer was operated at the wavelength of $70 \mu\text{m}$, while in the second one (Obs. ID of 1342235112 and 1342235113) the $100 \mu\text{m}$ filter was adopted for the blue camera.

We retrieved the final release of the SPIRE and PACS science products from the *Herschel* Science Archive. We analysed the data with version 15.0.1 of the HERSCHEL INTERACTIVE PROCESSING ENVIRONMENT, by applying the corresponding SPIRE and PACS calibration trees, SPIRE_CAL_14_3 and PACS_CAL_77_0, respectively.

We adopted the Level-2 science products for SPIRE imaging and photometry. For the PACS blue camera (i.e., 70 and 100 μm), we employed the Level-2.5 data, while we utilised the Level-3 products for the PACS red camera (160 μm). From the PACS image products, we analysed the HPPUNIMAP and HPPJSMAP maps, both of which are applicable to extended sources. We confirmed that the photometric results from the two maps were consistent with each other within 5 per cent. We, hereafter, adopt the HPPUNIMSP results because its photometric accuracy is slightly better at 70 μm .

2.2 FIR images

Figure 1 shows the 160 μm PACS (panel a) and 350 μm SPIRE (panel b) images around the radio galaxy Cygnus A on which the 5 GHz radio contours (Perley et al. 1984) are overlaid. The FIR emission from the nucleus of Cygnus A is significantly detected both in the PACS and SPIRE bands. The nucleus in the PACS image is saturated for clear visualisation of fainter emission associated with the hot spots D. The inset inserted into panel (a) of Figure 1 shows the image around the nucleus with a different colour scale. The PACS image was aligned with the radio one by referring to the nucleus position to correct the astrometric error (≤ 1 arcsec for all the PACS bands). We ignored the astrometric error for all the SPIRE bands, because the typical astrometric uncertainty of *Herschel* (2 arcsec; Swinyard et al. 2010) is significantly smaller than the SPIRE pixel size (6–14 arcsec, dependent on the photometric band). The FIR sources associated with the radio hot spots A and D were clearly detected. In this paper, we focus on the FIR source corresponding to hot spot D because the hot spot A is reported to be subjected to bright emission surrounding it in the NIR and optical bands (Stawarz et al. 2007).

Firstly, we investigated the spatial property of the FIR source using the PACS image, which has a better angular resolution than that of SPIRE. Figure 2 shows the 160 μm PACS close-up view around hot spot D. The FIR source seems slightly extended in comparison to the PACS point spread function (PSF) with the size of $d_{\text{PSF}} = 11.4$ arcsec in the Full Width at Half Maximum (FWHM) at 160 μm , shown with the white circle in Figure 2. The radio image reveals the fainter hot spot E, ~ 5 arcsec to the west of hot spot D. Thus, in the PACS image, the FIR source is possibly contaminated by hot spot E.

In order to roughly evaluate of the size of the FIR source, we firstly applied SUSSEXtractor (Savage & Oliver 2007) to the PACS data, by changing the apparent source size. No FIR source was found when the input source size was set to the PSF size. However, we detected the source for an input source size larger than the PSF size, except for a marginal detection at 70 μm . Table 1 summarises the PACS result of the source detection. Here, we calculated the apparent source diameter, d_{ap} , which gives the highest Signal-to-Noise (SN) ratio. The obtained source size ($d_{\text{ap}} = 13$ arcsec at 160 μm), which is larger than the PSF one ($d_{\text{PSF}} = 11.4$ arcsec in the FWHM), implies the possible source extension.

To measure the apparent source size more quantitatively, we fitted an axially symmetric two-dimensional Gaussian function with a flat offset to the PACS image of the source. Here, we analysed only the 160 μm image, since it gives the highest SN ratio among the three PACS bands. The central position of the Gaussian function is fixed at the source position derived by SUSSEXtractor. The FWHM apparent source size is evaluated as $d_{\text{fit}} = 14 \pm 1$ arcsec. It is confirmed that the apparent source size is larger than the PSF size. We deconvolved the PSF size from the obtained apparent source size as

$$d_{\text{src}} = \sqrt{d_{\text{fit}}^2 - d_{\text{PSF}}^2}. \text{ After the deconvolution, the derived source size}$$

($d_{\text{src}} = 8 \pm 2$ arcsec) becomes comparable to the angular separation between hot spots D and E.

The FIR source position determined by SUSSEXtractor is significantly shifted from radio hot spot D, and the angular offset of ($\Delta\theta_{\text{RA}}$, $\Delta\theta_{\text{Dec}}$) = $(-4.3 \pm 1.1, 0.8 \pm 1.1)$ arcsec at 160 μm is not negligible in comparison with the PSF size. In Figure 2, we show the FIR source position determined with SUSSEXtractor and the best-fit apparent source size (i.e., d_{fit}) with the black cross and dashed black circle, respectively. Although hot spot D is on the brightest pixel of the PACS image, the source is shifted toward radio hot spot E. Besides, the apparent source size encompasses both hot spots D and E. These imply the FIR emission mainly originates in hot spot D with a notable contamination from hot spot E. Both the deconvolved source size and the position offset implies some contamination from hot spot E.

The FIR source seems point-like in the SPIRE image displayed in panel (b) of Figure 1. The point-like nature of the FIR source in the SPIRE band seems reasonable, since the deconvolved source size with the PACS (i.e., 8 ± 2 arcsec at 160 μm) is smaller than the SPIRE PSF (see Table 1). Thus, we performed SUSSEXtractor by adopting the SPIRE PSF size. We significantly detected the source with an SN ratio is 70 in the 350 μm image. Table 1 also summarises the result of the SPIRE source detection. The derived angular offset of ($\Delta\theta_{\text{RA}}$, $\Delta\theta_{\text{Dec}}$) = $(-1.3 \pm 0.3, 1.6 \pm 0.3)$ arcsec at 250 μm is negligible in comparison with the PSF size of $d_{\text{PSF}} = 24$ arcsec even at 250 μm , where the spatial resolution is highest among the SPIRE photometric bands. Thus, we did not resolve hot spots D and E due to the SPIRE angular resolution.

2.3 FIR photometry

We measure the PACS and SPIRE flux of the FIR source associated with hot spot D. Since hot spot E is not fully resolved with the PACS and SPIRE, as shown in section 2.2, we here evaluate the sum flux of hot spots D and E by adopting aperture photometry. We decompose the source flux into those of D and E by utilising the multi-wavelength spectra in section 3.1.

The source and background apertures we adopted for the PACS photometry at 160 μm is shown in panel (a) of Figure 3, while those for the SPIRE photometry at 350 μm is indicated in panel (b). The radius of the source aperture for the individual SPIRE and PACS photometric bands is summarised in Table 2. For the SPIRE photometry, the FIR source position obtained from SUSSEXtractor is employed as the centre of the source aperture. The radius of the source aperture is determined to avoid contamination from the nucleus. To evaluate the spatial fluctuation of the background flux density, the six background apertures are selected from the region around the FIR source. We did not put any background aperture between the FIR source and nucleus to avoid contamination from the nucleus and possibly from the lobe. For the background regions, we adopted the same aperture radius as for the source one. At the 500 μm SPIRE band, we did not evaluate the FIR source flux, because the nuclear contamination is expected to be severe due to the poor angular resolution. For the PACS photometry, the radio position of hot spot D is employed as the source position, instead of that determined with SUSSEXtractor because it nearly coincides with the brightness peak of the FIR source on the PACS image. The source aperture size is determined to safely include the emission from hot spots D and E but excludes the nuclear contamination and diffuse emission possibly associated with the lobe. Similar to the SPIRE photometry, the same radius as for the source region is adopted for the background regions.

We performed the SPIRE and PACS photometry by using the individual background regions. Following the standard manner, we

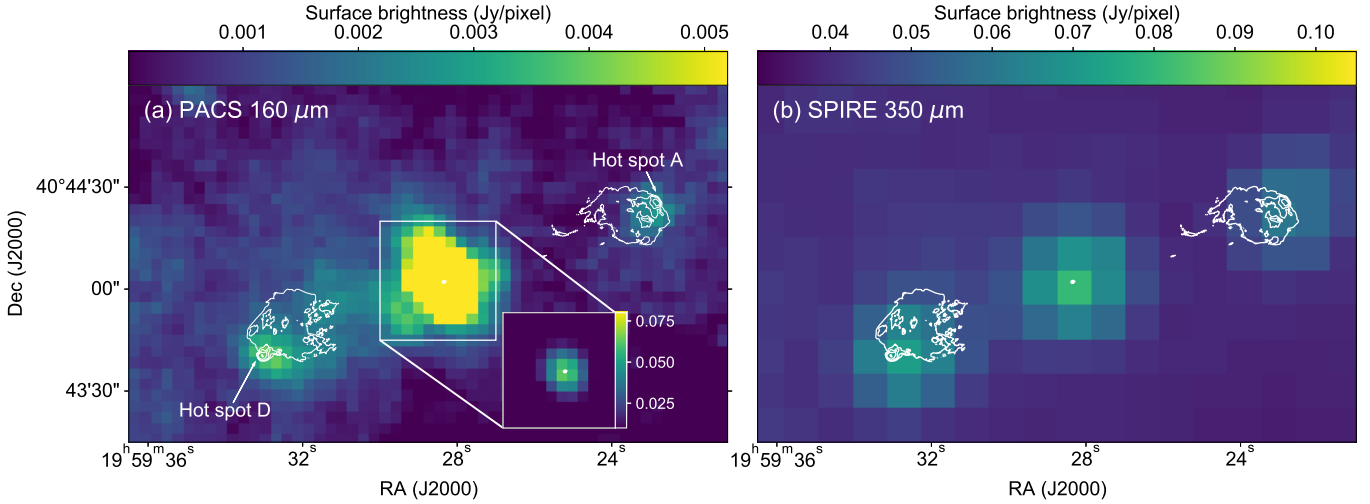


Figure 1. Panel (a) shows the 160 μm PACS image of Cygnus A. Panel (b) shows the 350 μm SPIRE image. On both panels, the 5 GHz radio contours (Perley et al. 1984) are overlaid. The coloured bar above each panel shows the surface brightness in the unit of Jy pixel^{-1} . The arrows in panel (a) show the hot spots A and D. The inset in panel (a) shows the PACS image in a different colour scale and VLA contours around the nucleus.

Table 1. Summary of the FIR source spatial properties derived with SUSSEXtractor

instrument	λ^a (μm)	d_{PSF}^b FWHM (arcsec)	$\Delta\theta_{\text{RA}}^c$ arcsec	$\Delta\theta_{\text{Dec}}^c$ arcsec	d_{ap}^d FWHM (arcsec)	SN ratio
SPIRE	500	35	-1.5 ± 0.4	3.5 ± 0.4	35 (fixed)	56
	350	24	-1.3 ± 0.3	1.6 ± 0.3	24 (fixed)	70
	250	18	-2.7 ± 0.4	1.0 ± 0.4	18 (fixed)	29
PACS	160	11.4	-4.3 ± 1.1	0.8 ± 1.1	13	7.4
	100	6.8	-2.5 ± 1.1	0.2 ± 1.1	12	6.7
	70	5.6	-2.5 ± 1.2	0.4 ± 1.2	9	4.5

a The effective wavelength

b The averaged PSF size, taken from the calibration tree

c The angular offsets of the FIR source from the brightness centre of hot spot D at 5 GHz.

d The apparent source size, for which the SN ratio of the source is maximised.

adopted the standard deviation of the fluxes of the six background regions as the photometric error. The aperture correction was performed to the measured flux densities by retrieving the correction factor for the adopted source radius from the calibration tree. We adopted the power-law (PL) spectrum with an energy index of $\alpha = 1$ for the colour correction. At least in the range of $\alpha = 1$ –2, the colour correction has only a minor contribution with a correction factor of < 1 and < 0.1 per cent for SPIRE and PACS, respectively. In Table 2, we summarise the aperture-and-colour corrected flux density (F_ν) of the FIR source in Table 2, together with the adopted correction factor (C_{cor}). The corrected flux densities are derived as $F_\nu = 199 \pm 58$ and 92.3 ± 13 mJy in the SPIRE 350 μm and the PACS 160 μm photometric bands, respectively.

We show the obtained FIR spectrum of the source in Figure 4. The FIR spectrum is successfully reproduced by the PL model ($\chi^2/\text{d.o.f.} = 3.55/3$), as shown with the dashed line in Figure 4. An energy index of $\alpha = 1.64 \pm 0.17$ and a flux density at 10^{12} Hz of 0.26 ± 0.04 Jy are obtained. Although the measured energy index is higher than that adopted for the colour correction ($\alpha = 1$), the difference in the correction factor between these indices is negligible.

Table 2. Summary of the SPIRE and PACS photometry

instrument	λ μm	ν^a 10^{11}Hz	aperture radius arcsec	C_{cor}^b	F_ν^c mJy
SPIRE	350	8.6	30	1.240	291 ± 66
	250	12	22	1.283	199 ± 58
PACS	160	19	12	1.49	92.3 ± 13
	100	30	12	1.29	50.7 ± 9.4
	70	43	12	1.25	12.6 ± 7.5

a The frequency corresponding to the effective wavelength of λ

b The correction factor including the colour and aperture correction

c The aperture and colour corrected flux density of the FIR source

3 SPECTRUM OF HOT SPOT D

3.1 Subtraction of the contamination from hot spot E

In order to investigate the spectral properties of the FIR source, we compare its FIR Spectral Energy Distribution (SED) with the radio and NIR data of hot spot D and E, taken from Lazio et al. (2006), Carilli et al. (1991), Wright & Birkinshaw (2004) and Stawarz et al. (2007). We show the radio to NIR SED of hot spots D and E in Figure 5. In the radio band, both hot spots D and E exhibit a flat SED with an energy index of $\alpha \sim 1$, while of hot spot D is brighter than that of hot spot E by an order of magnitude. Except for the 70 μm band, the obtained FIR flux is slightly higher than a simple PL extrapolation

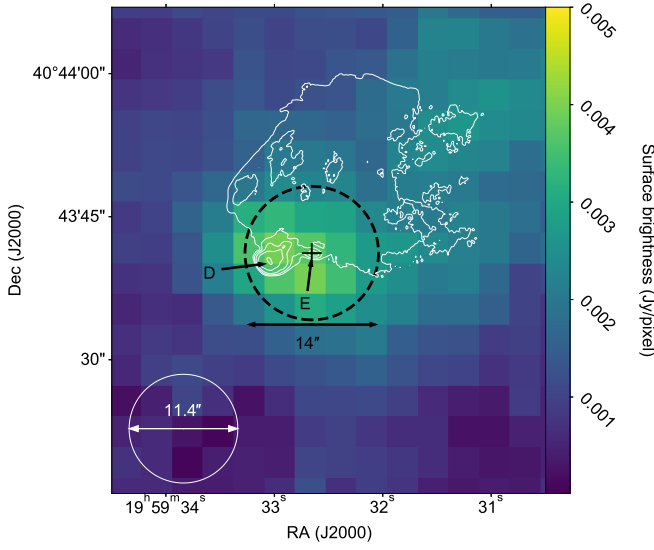


Figure 2. The $160\ \mu\text{m}$ image around the FIR source associated to hot spot D observed by the PACS. The black dashed circle and the black cross indicate the apparent source size and position obtained by SUSSExtractor, respectively. The black arrow below the dashed circle indicates the source size of 14 arcsec. The white solid circle shows the PSF size (11.4 arcsec) in the FWHM of PACS at $160\ \mu\text{m}$. The arrows labeled as D and E indicate the position of radio hot spots D and E, respectively.

of the radio flux from hot spot D. These results suggest that the FIR flux of the source is dominated by the emission from hot spot D with a possible contamination from hot spot E.

To subtract the contamination from hot spot E, we estimate the FIR spectrum of hot spot E by interpolating the radio and NIR spectrum. hot spot E has a lower NIR flux than the simple PL extrapolation of the radio spectrum. Thus, we fitted the radio to NIR spectrum of hot spot E with the cut-off power law (CPL) model described as $F_\nu \propto \nu^{-\alpha} \exp(-\nu/\nu_c)$, where ν_c denotes the cut-off frequency. The dashed line in Figure 5 shows the best-fit CPL model ($\chi^2/\text{d.o.f.} = 6/3$), with the flux density at 10 GHz of $F_\nu(10\ \text{GHz}) = 1.8 \pm 0.1\ \text{Jy}$, the energy index of $\alpha = 0.97 \pm 0.04$, and the cut-off frequency of $\nu_c = (1.1 \pm 0.4) \times 10^{13}\ \text{Hz}$. The evaluated FIR flux density of hot spot E ($F_{\nu, \text{E-fit}}$) is about 10 per cent of the FIR flux density obtained from the aperture photometry (i.e. $F_{\nu, \text{E-fit}}/F_\nu \sim 0.1$), except for at $70\ \mu\text{m}$ with $F_{\nu, \text{E-fit}}/F_\nu = 0.3$. By subtracting the flux of hot spot E from the measured FIR flux (F_ν), we estimated the FIR flux of hot spot D (i.e., $F_{\nu, \text{D}} = F_\nu - F_{\nu, \text{E-fit}}$). We summarise $F_{\nu, \text{D}}$ and $F_{\nu, \text{E-fit}}$ in Table 3. At the $160\ \mu\text{m}$ PACS band, the FIR fluxes of hot spots D and E are evaluated as $F_{\nu, \text{D}} = 83 \pm 13\ \text{mJy}$ and $F_{\nu, \text{E-fit}} = 9.4 \pm 1.5\ \text{mJy}$. As a result of the subtraction of the contamination from hot spot E, the derived FIR spectrum of hot spot D seems to smoothly connect to the radio spectrum within the errors, except for the $70\ \mu\text{m}$ band (see Figure 6).

3.2 Spectral modelling of hot spot D

We investigate the spectral properties of hot spot D. Figure 6 clearly shows that a simple PL does not reproduce the radio to NIR spectrum. Therefore, we first tried a CPL model to the observed spectrum, and derived the parameters as listed in Table 4. Although the CPL model, indicated with the dashed line in panel (a) of Figure 6, is statistically acceptable ($\chi^2/\text{d.o.f.} = 6.78/8$), we noticed several discrepancies between the observed and model spectra. The best-fit CPL mode seems

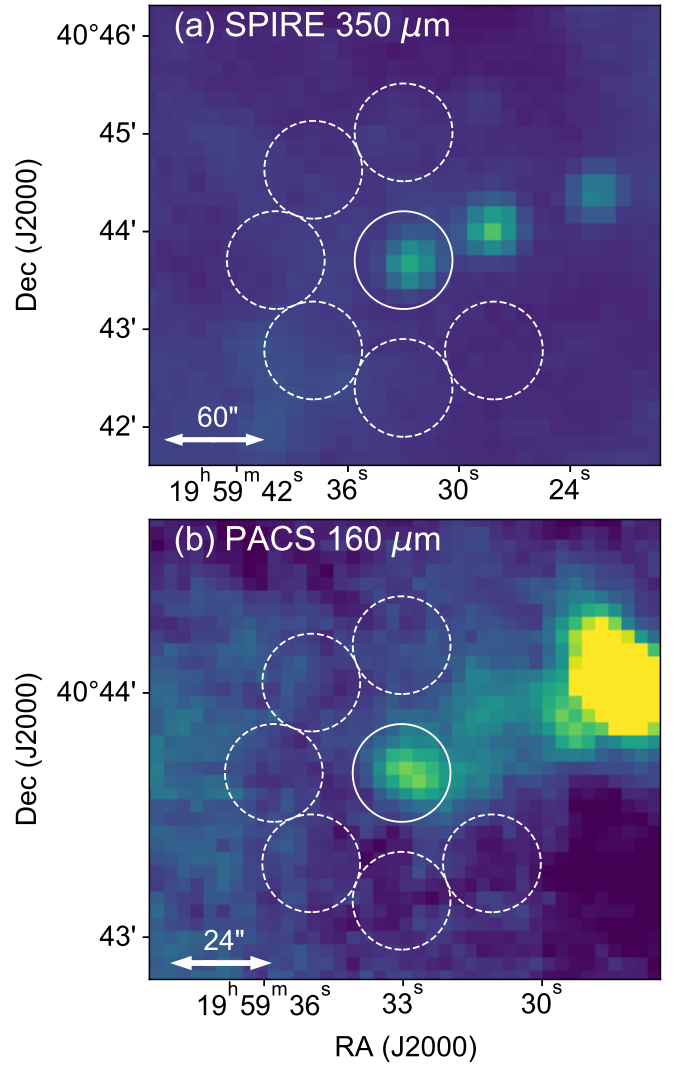


Figure 3. The source and background apertures used for the photometry with SPIRE (panel a) and PACS (panel b). The solid circle indicates the source aperture with a radius of 30 and 12 arcsec in $350\ \mu\text{m}$ and $160\ \mu\text{m}$ images, respectively. The dashed circles correspond to the background apertures with the same radius as the source one. The white arrows indicate the aperture diameter.

slightly flatter than the observed FIR spectrum of hot spot D, and hence, it possibly overestimates the $70\ \mu\text{m}$ flux. This result suggests a spectral break in the FIR band.

In order to evaluate the possible break, we next adopted a broken PL model, subjected to a high energy cut-off written as

$$F_{\nu, \text{D}} \propto \begin{cases} \nu^{-\alpha} \exp(-\nu/\nu_c) & \text{for } \nu < \nu_{\text{br}} \\ \nu^{-(\alpha+\Delta\alpha)} \exp(-\nu/\nu_c) & \text{for } \nu > \nu_{\text{br}}, \end{cases} \quad (1)$$

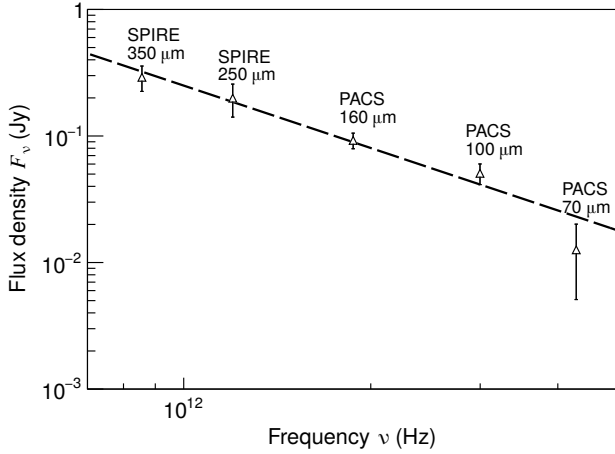
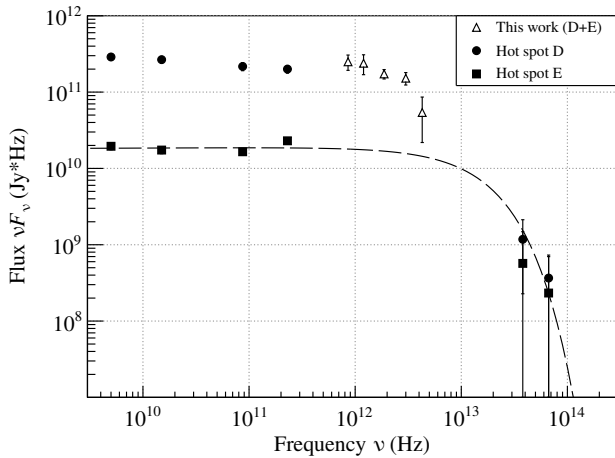
Hereafter, we simply refer to the model as the Broken PL (BPL) model. We fitted the spectrum with the BPL model and found that the model improved the fitting. However, due to the degeneracy between the change of the energy index ($\Delta\alpha$) and the break frequency (ν_{br}), it is difficult to determine the parameters simultaneously. Thus, we searched for the range of $\Delta\alpha$ in which the fit is significantly improved. As a result, we found that in the range of $0.23 < \Delta\alpha < 7$, the model reduces the chi-square by at least 1 in comparison to the CPL model. Therefore, we fixed the index change at $\Delta\alpha = 0.5$ to constrain the

Table 3. Estimated Flux densities of hot spot D and E.

instrument	λ μm	ν 10^{11} Hz	$F_{\nu, \text{E-fit}}^a$ mJy	$F_{\nu, \text{D}}^b$ mJy
SPIRE	350	8.6	22.0 ± 2.9	269 ± 66
	250	12	15.4 ± 2.2	185 ± 58
PACS	160	19	9.4 ± 1.5	83 ± 13
	100	40	5.3 ± 1.0	45.4 ± 9.4
	70	43	3.4 ± 0.7	9.2 ± 7.5

^a The FIR flux density of hot spot E calculated from the best-fit CPL model.

^b The FIR flux density of hot spot D calculated as $F_{\text{D}} = F_{\text{cor}} - F_{\text{E,fit}}$

**Figure 4.** The FIR spectrum of the source associated with hot spot D obtained in the PACS and SPIRE photometry, before subtracting the contamination from hot spot E. The open triangles show the flux density of the source, while the dashed line presents the best-fit PL model, with the best-fit energy index of $\alpha = 1.64 \pm 0.17$.**Figure 5.** Broadband SED of hot spot D and E. The open triangles show the SED of the FIR source associated with hot spot D with the contamination from the hot spots included, obtained in this work. The filled circles and filled squares show the spectra of hot spots D and E (Lazio et al. 2006; Wright & Birkinshaw 2004; Stawarz et al. 2007), respectively, in the radio and NIR bands. The dashed line displays the best-fit CPL model to the spectrum of hot spot E.

break frequency, since it is theoretically consistent with the index change predicted from the diffusive shock acceleration under the continuous energy injection, accompanied with a radiative cooling (Heavens & Meisenheimer 1987; Carilli et al. 1991). Stawarz et al. (2007) interpreted the spectrum of hot spot D, without the FIR data, by the BPL model with $\Delta\alpha = 0.5$, and derived the parameters denoted as "BPL (Stawarz)" in Table 4. Although the BPL model with the parameters by Stawarz et al. (2007) agrees with the radio data, it significantly underestimates the FIR spectrum, as shown with the dash-dotted line in panel (a) of Figure 6. This suggests that the break frequency is higher than their result ($\nu_{\text{br}} = 0.5 \times 10^{12}$ Hz; Stawarz et al. 2007).

To determine precisely the break frequency, we re-fitted the BPL model to the spectrum of hot spot D, by including the FIR data. The dashed line in panel (b) in Figure 6 shows the best-fit BPL model ($\chi^2/\text{d.o.f.} = 4.8/7$), which successfully reproduces the overall spectrum in the radio, FIR and NIR ranges. The best-fit parameters are summarised in Table 4. By adopting the BPL model, the fit is slightly improved compared to the CPL model; the null-hypothesis probability of the F -test between the best-fit CPL and BPL is 14 per cent. The best-fit break frequency is determined as $\nu_{\text{br}} = 2.0^{+1.2}_{-0.8} \times 10^{12}$ Hz. The derived break frequency is significantly higher than that adopted in Stawarz et al. (2007). The other parameters are found to stay almost unchanged from those of the CPL model and those of the BPL model in Stawarz et al. (2007). Thanks to the FIR data, we have succeeded in determining the break frequency of hot spot D for the first time.

4 DISCUSSION

4.1 FIR Evidence of the cooling break

We detected the FIR emission associated with hot spot D, located where the eastern jet of the radio galaxy Cygnus A terminates, in the 70–350 μm images obtained by the *Herschel*/SPIRE and PACS. This is the second hot spot detected in the FIR range after the west hot spot of Pictor A (Isobe et al. 2020). After subtracting the contamination from hot spot E, the FIR spectrum of hot spot D is revealed to be consistent with the extrapolation from the radio PL spectrum. Therefore, the FIR emission is naturally attributed to the synchrotron emission from the same electron population producing for the radio emission.

In the radio to FIR range, the spectral energy index is derived as $\alpha \approx 1.1$. Although the index is explainable by the diffusive shock acceleration (Bell 1978), it is larger than the canonical value, $\alpha = 0.5$, corresponding to the strong non-relativistic shock. Several possible ideas for the spectral softening are presented in Stawarz et al. (2007), including some relativistic effects and/or magnetic-field configurations, and thus, we did not discuss this issue any further in the present

Table 4. Best-fit parameters to the synchrotron spectrum of hot spot D.

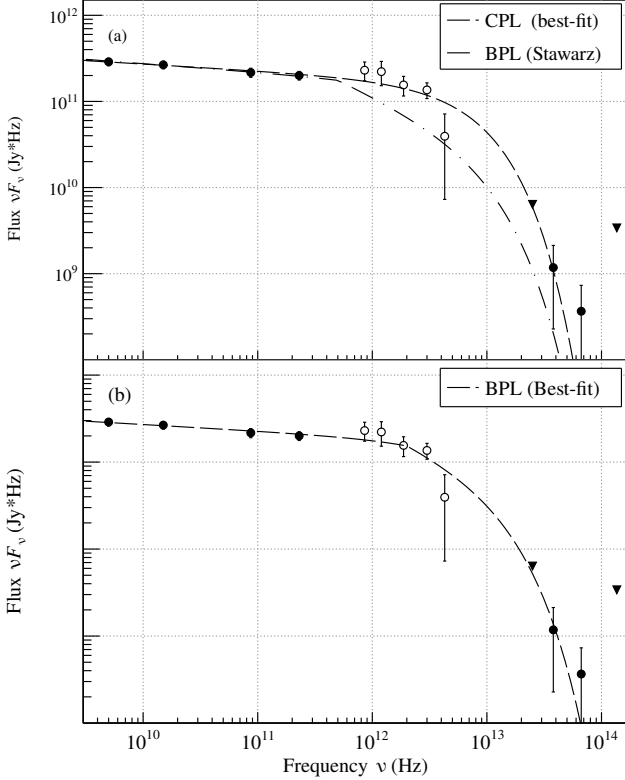
model	$F_\nu(10 \text{ GHz})^a$ Jy	α^b	ν_{br}^c Hz	ν_c^d Hz	$\chi^2/\text{d.o.f.}$
CPL	27 ± 1.7	1.06 ± 0.03	—	$(0.8 \pm 0.1) \times 10^{13}$	6.7/8
BPL (Stawarz) ^e	27	1.1	0.5×10^{12}	0.9×10^{13}	20/11
BPL ^e	27 ± 1.8	1.07 ± 0.03	$2.0^{+1.2}_{-0.8} \times 10^{12}$	$(1.2 \pm 0.3) \times 10^{13}$	4.8/7

a The flux density at 10 GHz

b The energy index at lower frequency than the break and cut-off

c The break frequency of the BPL model

d The cut-off frequency

e The energy-index change is fixed as $\Delta\alpha = 0.5$.**Figure 6.** SED of hot spot D. The open circles show the FIR spectrum of hot spot D (F_D), after subtracting the contamination from hot spot E. The filled circles show the radio and NIR spectrum of hot spot D from literature. The dashed and dash-dotted line in panel (a) show the best-fit CPL model and the BPL model in Stawarz et al. 2007, respectively. The dashed line in panel (b) shows the best-fit BPL model.

paper. The synchrotron spectral shape at the higher frequency end depends on physical conditions associated with the acceleration region. Several models, including a simple one-shot energy-injection one, exhibit a high-frequency cut-off at the frequency corresponding to the maximum energy of the accelerated electrons. In contrast, the diffusive shock acceleration under a continuous injection (Meisenheimer et al. 1989; Carilli et al. 1991) predicts a spectral break with $\Delta\alpha = 0.5$ due to radiative cooling, in addition to the high-frequency cut-off. By filling the gap between the radio and NIR bands with the FIR data, we, for the first time, confirmed that the BPL model with $\Delta\alpha = 0.5$ better reproduces the observed synchrotron spectrum of the object than the CPL one. This indicates that

diffusive shock acceleration under continuous energy injection is the dominant acceleration process in hot spot D.

Previous studies tried to estimate the cooling break frequency of hot spot D, though they were not conclusive. Carilli et al. (1991) proposed the break feature in the GHz range as the cooling break. However, theoretical studies found that a cooling break at higher frequency than GHz is preferred in hot spots (e.g., Kino & Takahara 2004). In addition, Stawarz et al. (2007) clearly demonstrated that the GHz break feature does not represent the cooling break, since they precisely evaluated the spectral index change at the GHz feature as $\Delta\alpha \approx 0.8$, which is inconsistent with the cooling break (i.e., $\Delta\alpha = 0.5$), by re-analysing the high-resolution radio data. Instead, Stawarz et al. (2007) assumed a cooling break at the frequency of $\nu_{\text{br}} = 0.5 \times 10^{12}$ Hz to reproduce the spectrum they obtained. However, they were unable to justify this assumption because the frequency falls in the spectral gap between the radio and NIR ranges. We overcame this difficulty by introducing the newly obtained FIR data with *Herschel*. Thus, we have succeeded in directly measuring the cooling break as $\nu_{\text{br}} = 2.0^{+1.2}_{-0.8} \times 10^{12}$ Hz.

4.2 Magnetic-field estimation

In this section, we evaluate the magnetic field strength B in hot spot D. First, we constrain the magnetic field strength B as a function of the observed radius of the hot spot, R . Next, we re-evaluate the observed X-ray spectrum with the Synchrotron-Self-Compton (SSC) process to obtain an independent constraint on B and R from the cooling break. Finally, by combining these two considerations, we precisely determine the magnetic field strength in hot spot D.

4.2.1 Constraint from the cooling break frequency

From the cooling break frequency, we measure the magnetic field strength B as the function of the radius R . The cooling break is determined by mutual balance between an electron radiative cooling time scale, $t_{\text{syn}} = \frac{6\pi m_e c}{B^2 \sigma_T \gamma}$ and an adiabatic loss time scale, $t_{\text{ad}} = \frac{2R\eta}{\beta c}$, where m_e , c , σ_T , γ and β are the electron rest mass, speed of light, Thomson cross section, electron Lorentz factor, and downstream flow velocity behind the shock in the shock frame. The parameter η is a correction factor from the physical to effective lengths along the jet (i.e., $0 < \eta \leq 1$). This parameter simply quantifies non-uniformity in the post-shock region, and is equivalent to the filling factor of the magnetic field. Here, for simplicity, the Compton cooling is neglected based on the relative observed strength of the synchrotron and SSC components. Because the two time scale becomes equal to each other at the cooling break, the Lorentz factor at the cooling break is given

by

$$\gamma_{\text{br}} = \frac{3\pi m_e c^2 \beta}{\sigma_T \eta R B^2}, \quad (2)$$

(Inoue & Takahara 1996). For high energy electrons above the cooling break, $\gamma > \gamma_{\text{br}}$, the synchrotron spectral slope changes by $\Delta\alpha = 0.5$, assuming that the energy injection is constant in time. The synchrotron frequency corresponding to the break Lorentz factor is derived as $\nu_{\text{br}} = \frac{3eB\gamma_{\text{br}}^2}{4\pi m_e c}$, where e is the elementary charge. Thus, the magnetic field B is estimated from the break frequency as

$$B = \left(\frac{27\pi m_e c^3 \beta^2}{4\sigma_T^2} \eta^{-2} R^{-2} \nu_{\text{br}}^{-1} \right)^{1/3} \\ \simeq 190 \mu\text{G} \times \left(\frac{\beta}{1/3} \right)^{2/3} \eta^{-2/3} \left(\frac{R}{1 \text{ kpc}} \right)^{-2/3} \left(\frac{\nu_{\text{br}}}{10^{12} \text{ Hz}} \right)^{-1/3}, \quad (3)$$

This method was successfully applied to estimate the magnetic field in blazars (e.g., Inoue & Takahara 1996; Kataoka et al. 2000) and hot spots, including the west hot spot of Pictor A (Isobe et al. 2020).

Here, as a baseline scenario, we adopted a uniform one-zone model ($\eta = 1$) with an ideal strong relativistic shock ($\beta = 1/3$; e.g., Kirk & Duffy 1999). By substituting the observed break frequency, $\nu_{\text{br}} = 2.0_{-0.8}^{+1.2} \times 10^{12}$ Hz, in Equation 3, we derive the magnetic field as a function of the radius as,

$$B \simeq 150_{-20}^{+30} \times \left(\frac{R}{1 \text{ kpc}} \right)^{-2/3} \mu\text{G}. \quad (4)$$

The area enclosed by the thick blue lines in panel (a) of Figure 7 indicates the acceptable magnetic field given by Equation 4.

In order to further constrain the magnetic field from Equation 4, we evaluate the radius of the object from the previous studies (e.g., Harris et al. 1994; Wilson et al. 2000; Kino & Takahara 2004; Stawarz et al. 2007). We conservatively adopt the radius range of $0.8 \text{ kpc} < R < 1.6 \text{ kpc}$, which roughly covers the radius estimations in the previous studies. The lower limit corresponds to the radius adopted in Stawarz et al. (2007) based on the VLA high-resolution observation (Perley et al. 1984), while the upper one was derived from the X-ray image with *Chandra* (Wilson et al. 2000). The horizontally hatched area in panel (a) of Figure 7 shows the magnetic field for the adopted radius range. Thus, the magnetic field is determined as $B = 90\text{--}210 \mu\text{G}$ by using the cooling break.

4.2.2 Constraint from the X-ray spectrum

In order to constrain the magnetic field independently from the cooling break, we made a Synchrotron-Self-Compton (SSC) model (Band & Grindlay 1985) for the observed X-ray spectrum of hot spot D. The SSC model is widely adopted to interpret the X-ray spectra of numbers of hot spots, and to constrain their magnetic field (Wilson et al. 2000; Hardcastle et al. 2004; Kino & Takahara 2004; Kataoka & Stawarz 2005). In the SSC process, the flux ratio of the synchrotron to SSC components depends on the magnetic field and the radius of the source. Stawarz et al. (2007) estimated the magnetic field of hot spot D as $B = 270 \mu\text{G}$, by applying the SSC model to its X-ray spectrum for the fixed radius of $R = 0.8 \text{ kpc}$. We, here, re-modelled the X-ray spectrum of the object by the SSC process to constrain the magnetic field for the radius range of $0.8 \text{ kpc} < R < 1.6 \text{ kpc}$, as we adopted in the previous subsection.

We compiled the broadband SED of hot spot D, as shown in Figure 8. The FIR data are those we obtained in section 2 (See Table 3). The

radio, NIR, and X-ray data are taken from Stawarz et al. (2007), in which hot spot D is resolved from hot spot E with the high-resolution images. The synchrotron spectrum of this object is measured in a wide frequency range between the radio and NIR bands. As mentioned in section 4.1, the spectrum appears to exhibit a low-frequency cut-off feature around 10^9 Hz. Although the origin of this feature is under debate (Carilli et al. 1991; McKean et al. 2016; Stawarz et al. 2007), we do not discuss it any further in the present paper. Thus, we only examine the synchrotron spectrum above the minimum frequency of $\nu_{\text{min}} = 1.4 \times 10^9$ Hz. In contrast, the synchrotron spectrum shows the high frequency cut-off, of which the frequency is determined as $\nu_{\text{cut}} = (1.2 \pm 0.3) \times 10^{13}$ Hz, in addition to the cooling break, as discussed in section 3.2. This cut-off is attributed to the maximum electron energy. The X-ray spectrum significantly exceeds the extrapolation of the radio-to-NIR synchrotron spectrum. Therefore it is thought to be produced via the SSC process.

We calculated the synchrotron and SSC spectra to reproduce the observed radio-to-X-ray SED. For the calculation, the open source package of NAIMA version 0.9.1 (Zabalza 2015) was utilised. Based on the observed shape of the synchrotron spectrum in the range of $\nu > \nu_{\text{min}}$, the input electron spectrum is assumed to be simply described by a broken power-law model as shown below;

$$N_e(\gamma) = N_0 \times \begin{cases} \left(\frac{\gamma}{\gamma_{\text{min}}} \right)^{-p} & \text{for } \gamma_{\text{min}} \leq \gamma < \gamma_{\text{br}} \\ \left(\frac{\gamma_{\text{br}}}{\gamma_{\text{min}}} \right)^{-p} \times \left(\frac{\gamma}{\gamma_{\text{br}}} \right)^{-(p+1)} & \text{for } \gamma_{\text{br}} \leq \gamma \leq \gamma_{\text{max}} \\ 0 & \text{otherwise,} \end{cases} \quad (5)$$

where N_0 , p , γ_{min} , and γ_{max} are the normalisation in the unit of the electron number per unit Lorentz factor, the spectral energy index, the minimum and maximum electron Lorentz factors, respectively. Thus, it is necessary to specify the seven parameters to simulated the overall spectrum; i.e., B , R , N_0 , p , γ_{min} , γ_{br} and γ_{max} .

Here, the SSC model calculation is performed for our baseline scenario, while the impact of the parameter η is discussed in §4.2.5. Through the following procedures, we check if a certain pair of B and R is able to reproduce the observed SED shown in Figure 8. Based on the synchrotron energy index of $\alpha = 1.07$ between the radio and FIR bands determined in section 3.2, the electron spectral index of $p = 2\alpha + 1 = 3.14$ is adopted. The minimum and cut-off synchrotron frequencies, ν_{min} and ν_{cut} respectively, are transformed into the minimum and maximum Lorentz factors, γ_{min} and γ_{max} , as $\gamma = \sqrt{\frac{4\pi m_e c \nu}{3qB}}$. In order to keep consistency to B and R , we adopted the break Lorentz factor calculated from Equation 2 instead of the observed value. We determine the electron normalisation N_0 so that the simulated synchrotron flux reproduces the observed one as $F_{10 \text{ GHz}} = 27 \text{ Jy}$ at 10 GHz (Stawarz et al. 2007). With these parameters, we compared the SSC model spectrum with the observed X-ray spectrum. If the calculated flux agrees with the observed X-ray one at 1 keV , $F_X = 47.0 \pm 5.9 \text{ nJy}$ (Stawarz et al. 2007), the input B - R pair is regarded as viable. We iterate these procedures for a wide range on the B - R plane. We show the synchrotron and SSC spectra for some representative values of B and R (i.e., Cases 1–3) in Figure 8 and tabulated the parameters in Table 5.

The area enclosed by the two thick black solid lines in Figure 7 indicates the acceptable values of the magnetic field and radius. As discussed in Section 4.2.1, we adopted the additional constraint on the radius as $0.8 \text{ kpc} < R < 1.6 \text{ kpc}$. Thus, we finally obtained the black vertically hatched area in panel (a) of Figure 7, within which

the observed 10 GHz radio and 1 keV X-ray fluxes are consistently described with the synchrotron and SSC components, respectively.

4.2.3 Magnetic field determination

By combining the investigation into the cooling break and the SSC modelling of the X-ray spectrum, shown in sections 4.2.1 and 4.2.2 respectively, we tightly constrained the magnetic field strength in hot spot D, for our baseline scenario. The derived B - R conditions from the individual considerations overlap with each other in the blue filled region in Figure 7, covering magnetic field strength of $B = 120$ – 150 μG for radii in the range $R = 1.3$ – 1.6 kpc. This is the most stringent magnetic-field constraint ever achieved for hot spots of radio galaxies (e.g., Hardcastle et al. 2004; Kataoka & Stawarz 2005).

In order to visually validate the magnetic-field estimation, the synchrotron and SSC model spectra are plotted in Figure 8 for three representative cases (Cases 1, 2, and 3). As shown with the filled circle in panel (a) of Figure 7, Case 1 ($B=130$ μG and $R=1.5$ kpc) simultaneously satisfies the two constraints. Therefore, the observed cooling break and X-ray flux are successfully reproduced by the synchrotron and SSC model components, respectively, as displayed with the thick solid lines in Figure 8. Case 2 ($B=270$ μG and $R=0.8$ kpc), plotted with the filled box in panel (a) of Figure 7, is located within the acceptable region for the X-ray spectrum, but outside the region for the cooling break. The parameters of Case 2 were adopted in Stawarz et al. (2007). The dashed line in Figure 8 clearly shows that the SSC model flux agrees with the observed X-ray one, although the cooling break frequency predicted by the model is lower than the observed value, causing the model synchrotron spectrum to fall below the observed spectrum in the FIR. The filled triangle in panel (a) of Figure 7 points to the parameters of Case 3 ($B = 160$ μG and $R = 1.0$ kpc), which only meets the cooling break condition. Thus, the simulated synchrotron spectrum is compatible with the observed cooling break, though the SSC model overestimates the X-ray flux, as depicted with the dashed line in Figure 8.

With the cooling break properly taken into account in the SSC model, we have succeeded in strongly constraining the magnetic field in hot spot D of Cygnus A ($B=120$ – 150 μG). If this method is systematically applied to the other hot spots, their magnetic field is expected to be precisely measured. In fact, a number of hot spots are suggested to exhibit the cooling break in the FIR range, because their magnetic field and radius are typically evaluated in the range of $B = 100$ – 500 μG and $R = 0.3$ – 3 kpc (e.g. Kataoka & Stawarz 2005; Zhang et al. 2018). In addition, Cheung et al. (2005) predicted that the cooling break is located around the FIR band for three optical hot spots, by simply connecting the radio and optical spectra with the broken PL model. Therefore, future FIR studies gives a powerful tool to evaluate the physical condition in the hot spots, by detecting the cooling break.

4.2.4 Energetics

We evaluated the energy densities of the non-thermal electrons and magnetic field, because these two components are directly accessible through the synchrotron radio and SSC X-ray radiations. Here, the physical parameters for Case 1 (see Table 5) are adopted, since the case satisfied both the cooling break and SSC constraints. The energy density of non-thermal electrons is calculated by integrating Equation 5 from γ_{\min} to γ_{\max} as $U_{\text{NT},e} = m_e c^2 \int_{\gamma_{\min}}^{\gamma_{\max}} \gamma N_e(\gamma) d\gamma \approx 2.9 \times 10^{-9}$ erg cm^{-3} . The energy density of the magnetic field is evaluated as $U_B = B^2/8\pi = 0.67 \times 10^{-9}$ erg cm^{-3} . The derived $U_{\text{NT},e}$ and

U_B values at hot spot D are consistent with the previous estimations by Stawarz et al. (2007); Snios et al. (2018). Thus, a non-thermal-electron dominance of $U_{\text{NT},e}/U_B \sim 4$ is indicated in hot spot D. A similar non-thermal-electron dominance is reported for the hot spot A, which is located at the west-jet terminal of Cygnus A (Kino & Takahara 2004).

4.2.5 Possible uncertainties

In this subsection, we evaluate the influence of possible deviations from our baseline scenario, adopted in sections 4.2.1 – 4.2.4. As is clear from equation (3), the magnetic field estimated from the cooling break is dependent on the adopted values of η and β . In addition, the parameter η has a possible impact on the SSC calculation, since it is related to the effective volume of the emission region. From the observational point of view, it is difficult to specify these two parameters. Therefore, we investigate the sensitivity of the magnetic field estimation to η and β .

Firstly, we deal with the effect of η , which is adopted to parameterize the post-shock non-uniformity. Numerical studies (e.g., Inoue et al. 2009) frequently imply a post-shock inhomogeneous condition with a highly entangled magnetic field. Such a non-uniformity, described as $\eta < 1$, is expected to enhance the magnetic field estimation via the cooling break, since equation (3) indicates $B \propto \eta^{-2/3}$. As an example of highly non-uniform cases, the magnetic field for $\eta = 0.5$ is plotted on panel (b) of Figure 7 with the blue hatched region. In comparison to our baseline scenario ($\eta = 1$) shown in panel (a) of Figure 7, the compatible region to the observed cooling break is shifted upward by a factor of ~ 1.6 on the B - R plane. In contrast, the effective volume of the emission region is proportional to η , on condition that only the non-uniformity along the jet is taken into consideration for simplicity. As a result, the magnetic field to reproduce simultaneously the observed radio and X-ray fluxes is thought to scale as $B \propto \eta^{-1/3}$. As shown with the black vertically hatched area in panel (b) of Figure 7, the magnetic field for $\eta = 0.5$ obtained from the SSC modelling is predicted to be enlarged by a factor of ~ 1.3 , compared with that for our baseline scenario. By combining these two considerations, it is found that a slightly wider range of the magnetic field as $B = 150$ – 310 μG becomes acceptable.

Secondly, we make a brief comment on the impact of the β , i.e., the down-flow velocity in the shock frame normalised to the light speed. The impact of β on the magnetic field estimation seems to be more straight forward than that of η , because β only affects the cooling break condition as $B \propto \beta^{2/3}$ (see equation (3)). By adopting $\beta > 1/3$ (e.g., in the case of the weak shocks), a higher magnetic-field value becomes acceptable, since only the blue hatched region moves upward in panel (a) of Figure 7. However, the β value significantly smaller than $1/3$, corresponding to such as non-relativistic cases, is expected to be unrealistic, since it extinguishes the overlap between the cooling-break and SSC constraints on the B - R diagram, unless a significant non-uniformity is simultaneously considered.

4.3 Validity of the SSC scenario

When we estimated the magnetic field strength of hot spot D in Section 4.2, we simply assumed that all the observed X-ray flux is attributable to the SSC emission. Strictly speaking, there is no physical rationale for this assumption, although it is widely applied to X-ray studies of hot spots (Hardcastle et al. 2004; Kataoka & Stawarz 2005; Zhang et al. 2018). Actually, it is suggested that the X-ray spectrum of some optical hot spots is contaminated by other spectral components,

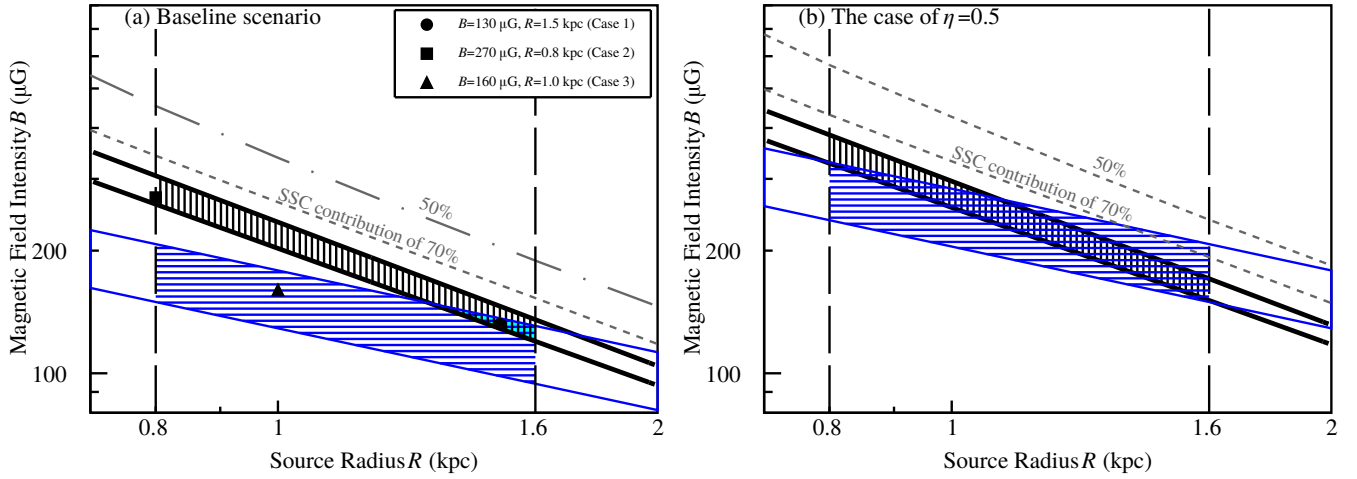


Figure 7. The magnetic field B and the radius R for hot spot D. The vertical dashed lines indicate the radius of $R = 0.8$ and 1.6 kpc. The constraints for our baseline scenario ($\eta = 1$ and $\beta = 1/3$) are displayed in panel (a), while those for $\eta = 0.5$ are plotted in panel (b) to visualise the sensitivity of the result on η (see section 4.2.5). The region enclosed by the blue solid line is the constraint from the FIR cooling break. Taking into account the previous results on the radius (the dashed lines; Perley et al. 1984; Wilson et al. 2000), the acceptable region is limited to the hatched region with the blue lines. The region hatched by the black vertical lines show the area matched to the SSC constraint with the radius condition considered. The cyan filled region indicates the parameters satisfying simultaneously the constraint from the cooling break and that from the SSC X-ray flux. The filled circle, filled square, and the filled triangle indicate Cases 1, 2, and 3, respectively, of which the parameters are listed in Table 5. The grey dash-dotted and dotted lines indicate the conditions where the SSC flux reproduces 50 and 70 per cent of observed X-ray flux, respectively.

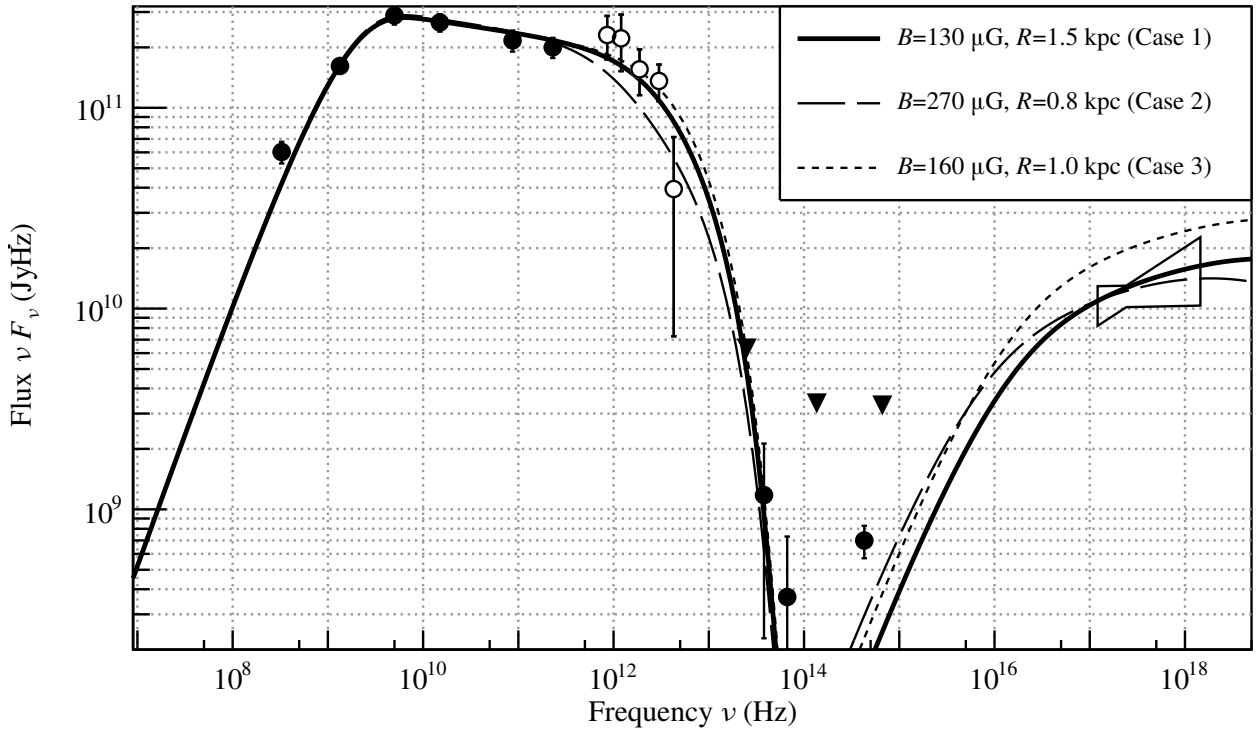


Figure 8. The broadband SED of hot spot D and the SSC model calculated in section 4.2.2. The open circles indicate the FIR spectrum obtained in this work. The black filled circles and the black filled triangles are the data points and upper limits (Stawarz et al. 2007 and references therein). The solid, dashed and dotted lines indicate the synchrotron+SSC models for Cases 1, 2, and 3, respectively.

Table 5. Parameters for the calculation of the synchrotron and SSC spectra

case	B μG	R kpc	P	N_0 particle per Lorentz factor	γ_{\min}	γ_{\max}	γ_{br}
Case 1	130	1.5	3.14	6.4×10^{56}	1.5×10^3	1.4×10^5	4.9×10^4
Case 2	270	0.8	3.14	4.4×10^{56}	1.1×10^3	9.9×10^4	2.1×10^4
Case 3	160	1.0	3.14	5.7×10^{56}	1.4×10^3	1.3×10^5	4.9×10^4

including the synchrotron emission from an additional electron population (Wilson et al. 2001; Hardcastle et al. 2007; Kraft et al. 2007; Perlman et al. 2010). As a by-product of the cooling break determined from the FIR data, we successfully quantitatively restrict the contribution of components different from the SSC one to the observed X-ray spectrum of hot spot D.

Compact synchrotron emitting sources, including the hot spots, are inevitably accompanied by some SSC emission. However, to determine the SSC flux, the observed X-ray spectrum may need to be corrected for contamination by other possible X-ray emission processes in the hot spot. The SSC model flux is predicted to scale, roughly, as $F_{\text{SSC}} \propto B^{-2}$, when the synchrotron flux is held fixed. Therefore, increasing the fraction of the contaminating spectral component requires the magnetic field to be enhanced and, hence, the $B-R$ region in Figure 7 allowed by the SSC model (i.e., the vertically hatched area) is shifted upward.

The dotted and dash-dotted lines in Figure 7 represent the $B-R$ relations, derived in a manner similar to that adopted in Section 4.2.2, for the cases where the SSC model reproduces 70 and 50 per cent of the observed X-ray flux, respectively. Such a small SSC contribution is clearly rejected in the case of our baseline scenario from panel (a) of Figure 7, because these two lines do not intersect the horizontally hatched region obtained by the cooling break consideration. In order for the regions from the cooling break and SSC conditions to overlap with each other, we found that the SSC fraction of higher than ~ 98 per cent of the best-fit X-ray flux (i.e., 47 nJy) is required. In the case of the lowest acceptable SSC fraction of 98 per cent, the regions from the two conditions cross at the top-right corner of the horizontally hatched region in panel (a) of Figure 7, which corresponds to the magnetic field of $B = 130 \mu\text{G}$ and the radius of $R = 1.6$ kpc, respectively. Even if the non-uniformity discussed in section 4.2.5 is assumed, the SSC dominance in the observed X-ray flux is still justified for a wide range of η , e.g., the SSC contribution of $\gtrsim 60$ per cent for $\eta = 0.5$ as shown in panel (b) of Figure 7.

In this way, we have put a very tight lower limit on the SSC contribution to the X-ray spectrum of hot spot D in the radio galaxy Cygnus A, owing to the detection of the cooling break. This result strongly indicates that the SSC emission significantly dominates the X-ray spectrum of this object. If the cooling break is systematically detected in the other hot spots, the SSC scenario for the hot spots' X-ray spectrum is possibly justified with high reliability.

5 SUMMARY

By making use of the *Herschel* SPIRE and PACS data, we have for the first time detected the FIR source associated with hot spot D in the radio galaxy Cygnus A. The important results and discussion derived from the FIR data are summarised below.

1. The spatial analysis revealed that the FIR source is extended with a PSF-deconvolved size of $d_{\text{src}} = 8 \pm 2$ arcsec, and its peak position is shifted by ~ 4 arcsec from hot spot D towards hot spot E. These properties indicate a significant contamination from hot

spot E. Thus, we first performed SPIRE and PACS photometry of the FIR source with a circle covering both hot spots D and E. The FIR of the source is evaluated as 291 ± 66 mJy and 92.3 ± 13 mJy at $350 \mu\text{m}$ and $160 \mu\text{m}$, respectively.

2. Since the FIR spectrum of the source is found to slightly exceed the extrapolation of the radio spectrum of hot spot D, the contamination from hot spot E is spectroscopically confirmed. By interpolating the radio and NIR spectra, the FIR flux of hot spot E was evaluated as ~ 10 per cent of the total FIR source flux. By subtracting the estimated FIR flux of hot spot E, the FIR flux of hot spot D was evaluated as 269 ± 66 mJy and 83 ± 13 mJy at $350 \mu\text{m}$ and $160 \mu\text{m}$, smoothly connecting the radio and NIR spectra of hot spot D.
3. The radio-to-NIR synchrotron spectrum of hot spot D is indicated to prefer the BPL model to the CPL one. The change in the spectral index of the BPL model becomes consistent with the prediction from the diffusive shock acceleration under the continuous energy injection, accompanied with a radiative cooling, i.e., $\Delta\alpha = 0.5$. Thanks to the FIR data, the break frequency was derived as $\nu_{\text{br}} = 2.0^{+1.2}_{-0.8} \times 10^{12}$ Hz, with the index change fixed at $\Delta\alpha = 0.5$. The break is naturally interpreted as the cooling break.
4. Based on the cooling break interpretation, the derived break frequency of hot spot D is converted into the magnetic field strength for the uniform one-zone model with the strong relativistic shock (i.e. $\eta = 1$ and $\beta = 1/3$). In addition to this estimation, we also evaluated the magnetic field strength by assuming that all the observed X-ray spectrum ($F_X = 47.0 \pm 5.9$ nJy at 1 keV; (Stawarz et al. 2007)) is attributable to the SSC process. By combining the two constraints, we determined the magnetic field intensity of hot spot D as $B = 120\text{--}150 \mu\text{G}$ for the radius of $R = 1.3\text{--}1.6$ kpc (panel a of Figure 7). This magnetic field strength indicates a non-thermal electron dominance with the electron-to-magnetic-field energy density ratio of $U_{\text{NT,e}}/U_B \sim 4$.
5. We discussed the impact of the possible deviation from the uniform one-zone model with the strong shock. If we adopted $\eta = 0.5$ for a representative case of a significant non-uniformity, the acceptable magnetic field strength is expected to become slightly higher as $B = 150\text{--}310 \mu\text{G}$, since the magnetic field from the cooling break scales as $\propto \eta^{-2/3}$ and that from the SSC model as $\propto \eta^{-1/3}$. The β value significantly smaller than $1/3$ is regarded as unrealistic, because the region which simultaneously meets the cooling-break and SSC constraints is expected to disappear.
6. If the observed X-ray flux is contaminated by emission processes different from the SSC one, the acceptable magnetic field is expected to be higher since the SSC flux is thought to scale as $F_{\text{SSC}} \propto B^{-2}$ for the fixed synchrotron flux. However, a detailed investigation into the cooling-break and SSC conditions indicates that the SSC fraction to the observed X-ray flux is higher than ~ 98 per cent in the case of the uniform one-zone model accompanied by the strong shock. Even if the deviation from this ideal assumption is considered, a high SSC dominance is found to be justified for a wide range of η (e.g., the SSC fraction of > 60 per cent for $\eta = 0.5\text{--}1$).

We have successfully constrained the physical parameters of hot spot D, especially magnetic field intensity, by determining the cooling break frequency in the FIR band. Based on this result, FIR observations are expected to be helpful to search for the cooling break feature in other hot spots.

DATA AVAILABILITY

The *Herschel* data utilised in this paper are available from the *Herschel* science archive.

ACKNOWLEDGEMENTS

Herschel is an ESA space observatory with science instruments provided by European-led Principal Investigator consortia and with important participation from NASA. This work was supported by JSPS KAKENHI Grant Numbers JP21K03635, JP21H01137 and JP18H03721. We thank Dr. Yukikatsu Terada, Dr. Kosuke Sato and Dr. Satoru Katsuta for their help in writing this paper.

REFERENCES

- Band D. L., Grindlay J. E., 1985, *ApJ*, **298**, 128
- Bell A. R., 1978, *MNRAS*, **182**, 147
- Bentley M., Haves P., Spencer R. E., Stannard D., 1975, *MNRAS*, **173**, 93P
- Brunetti G., Mack K. H., Prieto M. A., Varano S., 2003, *MNRAS*, **345**, L40
- Carilli C. L., Barthel P. D., 1996, *A&ARv*, **7**, 1
- Carilli C. L., Perley R. A., Dreher J. W., Leahy J. P., 1991, *ApJ*, **383**, 554
- Cheung C. C., Wardle J. F. C., Chen T., 2005, *ApJ*, **628**, 104
- Croston J. H., Ineson J., Hardcastle M. J., 2018, *MNRAS*, **476**, 1614
- Fanaroff B. L., Riley J. M., 1974, *MNRAS*, **167**, 31P
- Godfrey L. E. H., Shabala S. S., 2013, *ApJ*, **767**, 12
- Griffin M. J., et al., 2010, *A&A*, **518**, L3
- Hardcastle M. J., Birkinshaw M., Worrall D. M., 2001, *MNRAS*, **323**, L17
- Hardcastle M. J., Birkinshaw M., Cameron R. A., Harris D. E., Looney L. W., Worrall D. M., 2002, *ApJ*, **581**, 948
- Hardcastle M. J., Harris D. E., Worrall D. M., Birkinshaw M., 2004, *ApJ*, **612**, 729
- Hardcastle M. J., Croston J. H., Kraft R. P., 2007, *ApJ*, **669**, 893
- Harris D. E., Carilli C. L., Perley R. A., 1994, *Nature*, **367**, 713
- Harris D. E., et al., 2000, *ApJ*, **530**, L81
- Heavens A. F., Meisenheimer K., 1987, *MNRAS*, **225**, 335
- Hillas A. M., 1984, *ARA&A*, **22**, 425
- Inoue S., Takahara F., 1996, *ApJ*, **463**, 555
- Inoue T., Yamazaki R., Inutsuka S.-i., 2009, *ApJ*, **695**, 825
- Isobe N., Sunada Y., Kino M., Koyama S., Tashiro M., Nagai H., Pearson C., 2020, *ApJ*, **899**, 17
- Ito H., Kino M., Kawakatu N., Isobe N., Yamada S., 2008, *ApJ*, **685**, 828
- Kataoka J., Stawarz L., 2005, *ApJ*, **622**, 797
- Kataoka J., Takahashi T., Makino F., Inoue S., Madejski G. M., Tashiro M., Urry C. M., Kubo H., 2000, *ApJ*, **528**, 243
- Kawakatu N., Kino M., Takahara F., 2016, *MNRAS*, **457**, 1124
- Kino M., Kawakatu N., 2005, *MNRAS*, **364**, 659
- Kino M., Takahara F., 2004, *MNRAS*, **349**, 336
- Kino M., Kawakatu N., Takahara F., 2012, *ApJ*, **751**, 101
- Kirk J. G., Duffy P., 1999, *Journal of Physics G Nuclear Physics*, **25**, R163
- Kotera K., Olinto A. V., 2011, *ARA&A*, **49**, 119
- Kraft R. P., Birkinshaw M., Hardcastle M. J., Evans D. A., Croston J. H., Worrall D. M., Murray S. S., 2007, *ApJ*, **659**, 1008
- Lazio T. J. W., Cohen A. S., Kassim N. E., Perley R. A., Erickson W. C., Carilli C. L., Crane P. C., 2006, *ApJ*, **642**, L33
- McKean J. P., et al., 2016, *MNRAS*, **463**, 3143
- Meisenheimer K., Roser H. J., Hiltner P. R., Yates M. G., Longair M. S., Chini R., Perley R. A., 1989, *A&A*, **219**, 63
- Meisenheimer K., Yates M. G., Roeser H.-J., 1997, *A&A*, **325**, 57
- Owen F. N., Ledlow M. J., Morrison G. E., Hill J. M., 1997, *ApJ*, **488**, L15
- Perley R. A., Dreher J. W., Cowan J. J., 1984, *ApJ*, **285**, L35
- Perlman E. S., Georganopoulos M., May E. M., Kazanas D., 2010, *ApJ*, **708**, 1
- Pilbratt G. L., et al., 2010, *A&A*, **518**, L1
- Poglitsch A., et al., 2010, *A&A*, **518**, L2
- Savage R. S., Oliver S., 2007, *ApJ*, **661**, 1339
- Sikora M., Nalewajko K., Madejski G. M., 2020, *MNRAS*, **499**, 3749
- Smith D. A., Wilson A. S., Arnaud K. A., Terashima Y., Young A. J., 2002, *ApJ*, **565**, 195
- Snios B., et al., 2018, *ApJ*, **855**, 71
- Stawarz L., Cheung C. C., Harris D. E., Ostrowski M., 2007, *ApJ*, **662**, 213
- Steenbrugge K. C., Blundell K. M., Pyrzas S., 2014, *A&A*, **563**, A131
- Swinyard B. M., et al., 2010, *A&A*, **518**, L4
- Werner M. W., Murphy D. W., Livingston J. H., Gorjian V., Jones D. L., Meier D. L., Lawrence C. R., 2012, *ApJ*, **759**, 86
- Wilson A. S., Young A. J., Shopbell P. L., 2000, *ApJ*, **544**, L27
- Wilson A. S., Young A. J., Shopbell P. L., 2001, *ApJ*, **547**, 740
- Wilson A. S., Smith D. A., Young A. J., 2006, *ApJ*, **644**, L9
- Wright M. C. H., Birkinshaw M., 2004, *ApJ*, **614**, 115
- Yaji Y., Tashiro M. S., Isobe N., Kino M., Asada K., Nagai H., Koyama S., Kusunose M., 2010, *ApJ*, **714**, 37
- Zabalza V., 2015, in 34th International Cosmic Ray Conference (ICRC2015). p. 922 ([arXiv:1509.03319](https://arxiv.org/abs/1509.03319))
- Zhang J., Du S.-s., Guo S.-C., Zhang H.-M., Chen L., Liang E.-W., Zhang S.-N., 2018, *ApJ*, **858**, 27

This paper has been typeset from a \LaTeX file prepared by the author.